Title

Alleviating expansion-induced mechanical degradation in lithium-ion battery silicon anodes via morphological design

Authors

Gross, Sierra J
Hsieh, Meng-Ting
Mumm, Daniel R
et al.

Publication Date

2022-07-01

DOI

10.1016/j.eml.2022.101746

Peer reviewed

Extreme Mechanics Letters 54 (2022) 101746

Contents lists available at ScienceDirect

Extreme Mechanics Letters

journal homepage: www.elsevier.com/locate/eml

Alleviating expansion-induced mechanical degradation in lithium-ion battery silicon anodes via morphological design

Sierra J. Gross [a], Meng-Ting Hsieh [b], Daniel R. Mumm [a], Lorenzo Valdevit [a,b,*], Ali Mohraz [c,a,**]

[a] Department of Materials Science and Engineering, University of California, Irvine, 544 Engineering Tower, Irvine, CA 92697-2585, United States of America
[b] Department of Mechanical and Aerospace Engineering, University of California, Irvine, 4200 Engineering Gateway Building, Irvine, CA 92697-3975, United States of America
[c] Department of Chemical and Biomolecular Engineering, University of California, Irvine, 6000 Interdisciplinary Science and Engineering Building, Irvine, CA 92697-2580, United States of America

ARTICLE INFO

Article history:
Received 30 December 2021
Received in revised form 15 April 2022
Accepted 15 April 2022
Available online 29 April 2022

Keywords:
Lithium-ion battery silicon anode
Spinodal decomposition
Porous metal
Finite Elements Analysis (FEA)
Metamaterials
Triply periodic minimal surfaces (TPMS)

ABSTRACT

The mechanics of films undergoing volume expansion on curved substrates plays a key role in a variety of technologies including biomedical implants, thermal and environmental barrier coatings, and electrochemical energy storage systems. Silicon anodes for lithium-ion batteries are an especially challenging case because they can undergo volume variations up to 300% that results in cracking, delamination, and thus significant loss in performance. In this study, we use finite element analysis to model the volume expansion during lithiation for silicon coated on spinodal, inverse opal, gyroid, and Schwartz primitive nickel backbones and compare the distributions of maximum principal stress, strain energy density, and von Mises stress, which we use as indicators for propensity for cracking, delamination, and yielding, in order to explore the effect of backbone morphology on mechanical degradation during expansion. We show that, when compared to the inverse opal, the spinodal morphology reduces and uniformly distributes the maximum principal stress and strain energy density in the silicon layer, and delays the onset of expansion-induced yielding at all silicon layer thicknesses, which we ascribe to the unique interfacial curvature distribution of spinodal structures. This work highlights the importance of morphology on coatings undergoing volume variations and unveils the particular promise of spinodally derived materials for the design of next generation lithium-ion battery electrodes.

1. Introduction

The mechanics of curved films and coatings undergoing volume expansion plays a critical role in a number of technologies, ranging from electrochemical energy storage systems [1–6], to thermal and environmental barrier coatings [7–10] and biomedical implant coatings [11,12]. Lithium-ion batteries present a particularly challenging case, due to the large amount of active material expansion that can be experienced within their anodes during each charge cycle [13,14]. Alloying-type anodes are able to accommodate large amounts of lithium as they form a compound phase with the lithium ions that are electrochemically inserted [13,15]. These alloy-type anodes are currently the state of the art in Li-ion batteries due to their increased gravimetric and volumetric capacity, low discharge potential, and low toxicity [2,16]. Of the candidate materials considered, silicon (Si) has the highest theoretical capacity of 4200 $mAhg^{-1}$, over an order of magnitude greater than that of commercial intercalation-based graphite anodes [17–19]. However, during charge cycles, Si can undergo large volumetric variations (up to 300%) that can lead to cracking, pulverization, and delamination, resulting in overall loss in performance or even catastrophic failure [1,2,20].

Approaches to mitigating mechanical degradation caused by continued expansion and contraction have focused upon the design and development of composite electrode formulations [14,21–31], size reduction of active material domains [23–26,28,31–34], and control of the overall electrode microstructure [1,2,15,22,27,28,33–39]. Composite anodes – typically a mixture of carbon,

* Corresponding author at: Department of Materials Science and Engineering, University of California, Irvine, 544 Engineering Tower, Irvine, CA 92697-2585, United States of America.
** Corresponding author at: Department of Chemical and Biomolecular Engineering, University of California, Irvine, 6000 Interdisciplinary Science and Engineering Building, Irvine, CA 92697-2580, United States of America.
E-mail addresses: valdevit@uci.edu (L. Valdevit), mohraz@uci.edu (A. Mohraz).

https://doi.org/10.1016/j.eml.2022.101746

active material, and binder – are able to mitigate mechanical failure by way of reducing the overall volume variation and providing a soft medium to accommodate the expansion [14,21–29]. Nonetheless, their capacity suffers due to the lower fraction of active material [30,31,40]. Alternatively, the dimensions of the active Si structures can be reduced to form nanoscale architectures including nanosheets [27,41–43], nanowires [24,28], nanoparticles [23,25,26,32], and nanotubes [44–46], which have fast ion and electron transport, improved capacity, and the ability to reduce cracking and pulverization when below a critical size. However, these structures have low volumetric energy density, are difficult to scale, and often require complicated and expensive synthesis routes [20]. Lastly, the morphology of the electrode can also be designed, usually in conjunction with the other two strategies, to improve the volumetric energy density, structural stability, and ion and electron transport kinetics. Morphological design typically involves the reduction of the Si structures to the nanoscale to mitigate pulverization and the use of a conductive porous structure that provides space for lithiating Si to expand into, while enabling facile electron transport. One method to synthesize porous Si electrodes is to create building blocks of nanoscale Si below critical dimensions encapsulated in void-preserving carbon modified structures (Si@void@C) such as hollow carbon nanospheres [23] and tubes [43], or more complex pomegranate-inspired [26] and yolk-shell structures [27]. These methods take advantage of nanostructuring Si to reduce pulverization and C to increase conductivity, but they have nonideal ion transport pathways and require complex and difficult to scale synthesis protocols. Another route is to design 3D architectures with co-continuity of the pore and solid phases to ensure connected ion and electron transport pathways throughout the electrode. Examples include stochastic nanoscale Si networks coated in carbon (Si@C@void) with ant-nest-like [39] and coral-like [47] structures, but their synthesis routes do not allow for fine tuning of the morphology and the carbon coating provides minimal mechanical support. Alternatively, a conductive backbone, also serving as the current collector, with a thin active material coating can be used to improve the electrode's structural integrity [1,16,35]. In these cases, nickel (Ni) is commonly used as the skeletal backbone because of its mechanical stability, electronic conductivity, strong adhesion to Si, facile fabrication routes, low cost, and safety [1].

For thin Si coatings on a porous Ni backbone, the inverse opal (IO) represents one state-of-the-art architecture due to its regular pore arrangement, high specific capacity, and cyclability, as well as ease of fabrication and potential for scaleup [1,16,35]. Recent work has investigated how the salient design parameters such as the Si and Ni volume fractions, Si thickness, and characteristic pore size may be optimized to reduce the lithiation-induced stresses and improve the overall mechanical stability of an IO composite electrode [16]. In general, for films on a substrate, positive mean curvatures, especially with small radii of curvature, have been shown to intensify tensile or compressive deformation [3,16], facilitate and aggravate crack initiation and growth [3,16], increase buckle delamination [9], and promote circumferential propagation of delamination [5], while negative mean and gaussian curvatures can suppress the initiation and propagation of cracking [3,6] and delamination [5]. This can make the large-curvature regions of IO pore throats particularly susceptible to mechanical degradation, and due to the large volumetric expansion of the Si layer, these regions can also hinder ion transport pathways, ultimately limiting the cyclability and performance of these systems [16,35].

To ameliorate these challenges, here we propose a composite electrode with a co-continuous spinodal architecture. This choice is motivated by recent advances in the synthesis of composite materials with spinodal microstructure through thermodynamic instability growth mechanisms such as arrested spinodal decomposition in liquid mixtures, or dealloying of metals [48–52]. Owing to the kinetic pathway through which they are formed, these structures enjoy co-continuity, tunable and uniform domain sizes in the nm to hundreds of μm range, and negative gaussian and near-zero mean curvatures along their entire internal surface. Importantly, these synthesis routes are amenable to scaleup and self-assembly, allowing materials with spinodal microstructure to be produced in macroscopic quantities [53–57]. The unique morphological characteristics of spinodal materials have already been shown to improve the electrochemical performance of various systems including battery electrodes and gas-producing electrolyzers [58–60], as well as enhance the overall mechanical stability of porous constructs [57,61–66], and we theorize that the unique curvature distribution along their internal surfaces will help reduce cracking and delamination in systems undergoing large volumetric variations. To establish their potential benefits in mitigating mechanical degradation in Si-based Li-ion battery anodes, we utilize finite element analysis to compare the mechanical response of spinodal and IO composite electrodes, with Ni backbone and amorphous Si coating, at various states of volumetric expansion and with Si thicknesses between 50 and 150 nm. We focus on the distributions of the maximum principal stress and strain energy density as proxies for cracking and delamination, respectively [16,67–69], and unveil that the spinodal architecture provides important advantages over the IO in both contexts. We also analyze the yielding behavior of the Si layer to gain insights into the nonlinear phenomena that mediate stress distributions at high expansion ratios. Finally, to explain our findings, we compare our results to gyroid and Schwartz primitive architectures and demonstrate that the desirable behavior observed in the spinodal system stems from the unique curvature and distinctive microstructural features of minimal surface structures. While this work is presented in the context of Si-based electrodes for lithium-ion batteries, the results could provide insight for the design of other systems where thin films are subject to volumetric variations, such as observed with thermally grown oxides that develop on metals [70–73].

2. Methods

2.1. Generation of morphologies

Spinodal architectures and IOs can be fabricated via scalable synthesis routes and are therefore the focus of this study. The gyroid and Schwartz primitive are idealized mathematically defined surfaces that will primarily be used to explain how the morphological characteristics of the scalable models affect the mechanical response during expansion. The model morphologies and a summary of the characteristics interconnecting and differentiating them are provided in Fig. 1a. By comparing these structures, we will be able to understand the effects of minimal surface curvatures, periodicity, and pore size uniformity, since (1) the spinodal, gyroid, and Schwartz primitive are minimal surfaces, (2) the gyroid, Schwartz primitive, and IO are triply periodic, and lastly, (3) the spinodal and gyroid have uniform pore sizes throughout the structure, while the Schwartz primitive and IO are characterized by multiple pore sizes. Procedures used to generate the 3D morphologies are schematically shown in Fig. 1b and Fig.S1, and model and mesh parameters are listed in Table S1. Briefly, a shell structure for the minimal surface morphologies was generated from implicit equations and then the software package Simpleware ScanIP was used to create the Ni backbone, while the IO morphology was created directly in the commercial Finite Element package Abaqus CAE as described in more detail

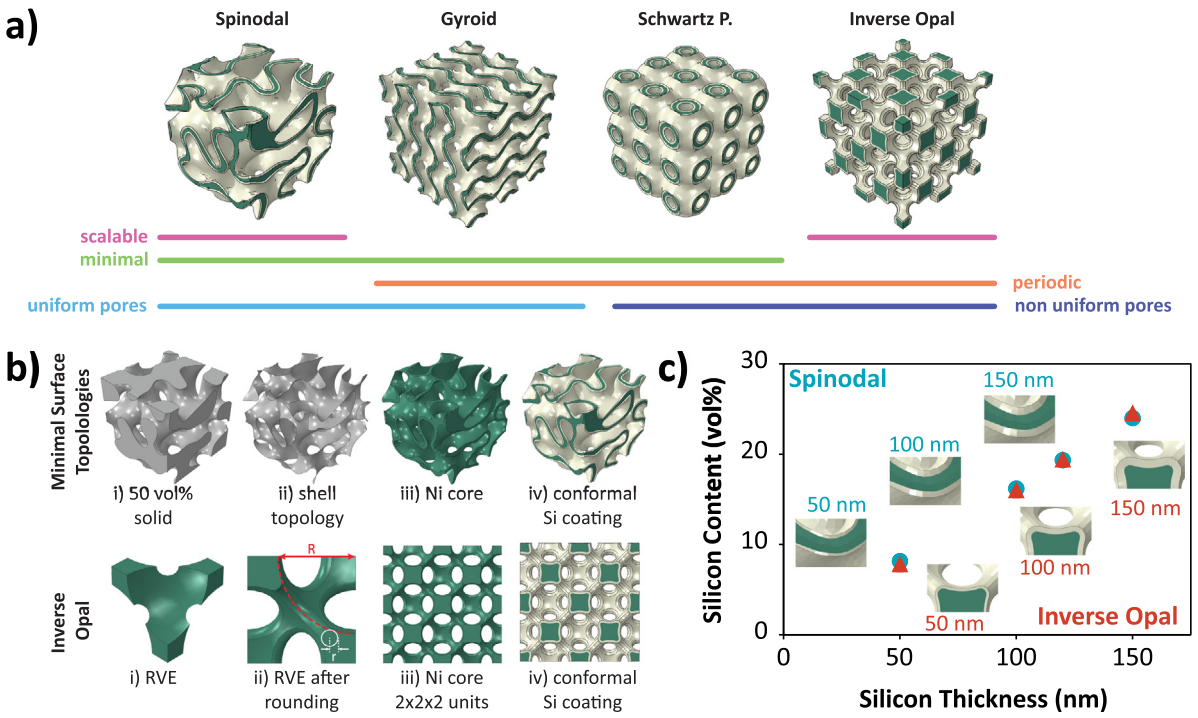

Fig. 1. Schematic of (a) model morphologies and characteristics, (b) model generation procedure for the minimal surface morphologies (top) and inverse opal with particle radius, R, and edge rounding radius, r, (bottom) and (c) silicon content vs. silicon layer thickness for the spinodal (blue circles) and inverse opal (red triangles) models. The green and tan phases represent the nickel metal scaffold and silicon active layer, respectively.

below. The number of unit cells and overall model sizes for the Ni backbones (Table S1) were tuned to achieve the same thickness and overall Ni volume fraction between the different morphologies. For each morphology, a conformal coating of Si was grown normal to the Ni surface of the models (Fig.S1), with 10 elements across the layer, using the Abaqus mesh editing tool for solid offset elements. For all models, the volume fraction of the Ni backbone was set to approximately 19 vol%. For the minimal surface morphologies, the Ni thickness was set to 2 μm. These values are achievable experimentally for shell-based structures [63], and balance the increase in mechanical stability and decrease in gravimetric capacity as the amount of electrochemically inactive material increases [16]. For Si, the thickness of the coating (t_{Si}) was varied between 50 and 150 nm. Within these ranges, the Si volume fraction is linearly proportional to the thickness for the spinodal and IO morphologies, as seen in Fig. 1c, with volume fractions in the experimentally relevant range between 8 and 24 vol% [16]. By matching the chemistries and volume fractions of the materials, comparable capacities would be expected. As such, we focus on the mechanical response and durability, where the differences in performance should be attributed to the morphology.

The spinodal morphology (Fig. 1b, top) was generated with the approach described in [61]: first, a 50% dense spinodal solid was numerically produced by solving the Cahn–Hilliard evolution equation within a Finite Difference framework [61,74]. The Cahn–Hilliard equation can be written as $\partial u/\partial t = \Delta^2\left[df(u)/du - \theta^2\Delta u\right]$, where $u(x, y, z, t)$ is the concentration of the solid and void phases at evolution time t and coordinate (x, y, z), $f(u) = 0.25\left(u^2-1\right)^2$ is a double-well free energy function, θ is the width of the transition between the two phases, and Δ is the Laplacian operator. The equation was solved at a dimensionless evolution time of 400,000 for a cubic domain with side length of 100 pixels, where the integration timestep was set to 0.005 and θ was set to 1 to achieve convergence and a smooth interface, respectively. The resulting volume was sectioned into a stack of 2D images and imported into the Simpleware ScanIP software where a spinodal shell was created from the image stack of the spinodal solid. The shell structures of the gyroid and Schwartz primitive morphologies were made directly in ScanIP using the implicit surface equations $sin(x)\,cos(y)+sin(y)\,cos(z)+sin(z)\,cos(x) = 0$ and $cos(x)+cos(y)+cos(x) = 0$, respectively. The Ni backbones for the minimal surface morphologies were created in ScanIP from their shell structures by adding a 1 μm thick Ni coating conformally to each side of the shells, for a total thickness of 2 μm. The IO representative volume element (RVE) was created directly in Abaqus as shown in the bottom of Fig. 1b. Starting from a cube with side lengths of 1.4 μm, the pores from templating particles were created by making revolution cuts at four corners with a radius (R) of 1.01 μm and then the sharp edges where the cuts overlapped were rounded with a radius (r) of 0.1 μm. The RVE was then patterned to create an IO backbone with 2 × 2 × 2 unit cells.

For each morphology, principal curvature maps were created for the Ni surface as follows. The mean (H) and gaussian (K) curvatures were extracted for each node on the surface with the MeshLab software built-in filter for discrete curvatures [75]. The principal curvatures, k_1 and k_2, were then calculated from the relationships $H = 0.5(k_1+k_2)$ and $K = k_1k_2$. The probability densities for the principal curvatures were then normalized by the number of nodes for each structure.

2.2. Mechanics and modeling approach

Abaqus CAE was used to simulate the mechanics of amorphous Si during lithiation for the various morphologies. Both Ni and Si were modeled as linear elastic/perfectly plastic solids. Young's modulus, Poisson's ratio, and yield strength for the Ni scaffold were set to 200 GPa, 0.3, and 600 MPa, respectively [16]. For Si, amorphous or crystalline phases could be used, but after the first cycle crystalline Si becomes amorphous [76]. To provide a more general understanding, the mechanical properties of amorphous

Si were used. The mechanical properties of Si vary with Li concentration because Si undergoes an atomistic structural change as the Si–Si bonds are broken and Li–Si bonds are formed [20,76]. This results in a softening effect where the Young's modulus, Poisson's ratio, and yield strength decrease from 90 GPa, 0.28, and 6.5 GPa for pure amorphous Si down to 34 GPa, 0.25, and 0.5 GPa for fully lithiated $Li_{3.75}Si$, respectively, as shown in Fig.S2 [77–80]. Assuming a stress-free state, the Si layer expands linearly with the concentration of Li up to 300 vol% [35,81,82]. Therefore, in this paper we will use the percentage of volumetric expansion to represent the extent of lithiation.

To simplify the analysis, we assume the concentration of Li to be uniform across the Si thickness at any given stage and simulate the lithiation process as a homogeneous isotropic thermal expansion in a quasi-static thermo-mechanical step, where the temperature is used as a proxy for the state of charge or percent lithiation, as established in previous literature [16,32,83]. This choice is justified by the extremely thin Si coatings considered here, which result in negligible concentration gradients across the Si layer. For example, the concentration change across a 160 nm Si coating during a fast charge rate of 2C was less than 0.5% [16]. While the concentration profile may not be completely uniform with very large C-rates and thick Si coatings, these simulations can still provide insight for the trends seen between the different morphologies, even under those less-practical conditions. For finite deformations, the thermal strain, ε^{th}, can be expressed as follows:

$$\varepsilon^{th} = \alpha \Delta T = \ln\left(L_f/L_i\right)$$

with α the thermal expansion coefficient, ΔT the applied temperature change, and L_i and L_f the initial and final linear dimensions of the specimen, respectively. Since Si undergoes a 300% volume change on a full charge [1,2,20], at full lithiation $L_f/L_i = \left(V_f/V_i\right)^{1/3} = (3)^{1/3}$. As the lithiation process is simulated by a temperature ramp from 0 to 1 ($\Delta T = 1$), we assign the Si elements an expansion coefficient, $\alpha = 0.3662$.

For a thin Si film, due to the strain mismatch between the Si coating and the underlying substrate, cyclic expansion and contraction can result in a buildup of large stresses that eventually lead to mechanical degradation. The specific modes of failure are highly dependent on the substrate, thin film and interfacial chemistries, morphology, and cycling conditions [84–86], but as schematically shown in Fig.S3, general cracking and delamination can lead to a loss of active material and connectivity, and thus drop in capacity. Modeling the complex non-linear phenomena that lead to electrode failure and the rate-dependent mechanical responses are daunting numerical challenges, which are well beyond the scope of this work. Nonetheless, valuable information on the impact of electrode morphology on its propensity to fail can be obtained by adopting the maximum principal stress (σ_{max}) and the total elastic strain energy density (W), in the Si domains as proxies for crack initiation and delamination, respectively, as established in previous work on mismatched coating and thin film systems such as thermal oxide barrier coatings undergoing cyclic thermal expansion [67,70,87–89].

The von Mises stress (σ_{vm}) was extracted for the spinodal and IO models with 100 nm Si thickness at each integration point in the Si layer and compared to the yield stress (σ_{y}) to capture the evolution of plastic deformation ($\sigma_{\mathrm{vm}} > \sigma_y$) as Si expands. The fraction of Si yielded for the spinodal and IO models with 50, 100, and 150 nm thickness at various stages of expansion were calculated as the number of Si integration points undergoing active yielding (AC yield = 1) normalized by the total number of integration points.

To decrease the computational load of the simulations, the following simplifications were made. Simulations for a spinodal morphology with a fine mesh of linear elements and coarse mesh of quadratic elements (Fig.S4) had nearly identical σ_{max} and W distributions, so linear elements were used for subsequent models, in order to reduce the simulation time without affecting the mechanical results. The Ni backbones for each morphology were composed of 300,000 or more C3D4 tetrahedral elements, and the Si coating was created from at least 800,000 C3D6 wedge elements, for a minimum total of 1 million elements for each model. The number of elements for each morphology can be found in Table S1. The simulations were solved using full integration elements and geometrically nonlinear analysis. In order to comply with the inherent non-periodicity of spinodal structures, periodic boundary conditions were not used. Instead, boundary conditions were applied to prevent translational movement in the x, y, and z directions for the nodes on the negative x, y, and z planes, respectively (Fig.S5). The number of unit cells for the IO models were set to $2 \times 2 \times 2$ based on a convergence study to minimize edge effects (Fig.S6). Based on additional convergence studies (Fig.S7 and Fig.S8), 10 elements were used across the Si coating thickness to balance the computational burden of the simulation with the accuracy achieved in the stress and strain gradients across the thickness. Lastly, the data was extracted from the inner regions of the models (defined individually for each morphology, shown in Fig.S9) in order to account for residual edge effects that cause stress concentrations near the boundaries.

3. Results and discussion

3.1. Effect of silicon expansion

To understand the effect morphology has on the mechanical response of Si during lithiation-induced expansion, σ_{max} (Fig. 2a), W (Fig. 2b), and σ_{vm} (Fig. 3a) will be analyzed for a spinodal (blue) and IO (red) model with t_{Si} of 100 nm. As local stress intensifications are strongly affected by mesh quality, boundary conditions, and local geometrical features, we choose to compare distributions over the entire Si domain as opposed to the extreme values alone. Fig. 2 compares σ_{max} and W, where the top graphs show the probability density, normalized by the area under the curve, for 30, 60, and 300 vol% expansion, with corresponding contours in the inset. The bottom graphs show whisker plots extracted from the distributions at various stages of volume expansion ranging from 30% to 300%, where the box denotes the 25th–75th percentile range, the internal line represents the median value, and the endcaps mark the 1st and 99th percentiles. To determine when yielding occurs, Fig. 3a plots the lithiation-dependent Si yield strength in relation to whisker plots of σ_{vm} for representative spinodal and IO models with t_{Si} of 100 nm. To understand the yielding behavior and effect of Si thickness for the two morphologies, Fig. 3b plots the percentage of Si yielded during lithiation for t_{Si} of 50 nm (dotted), 100 nm (dashed), and 150 nm (solid) where shaded regions are added to guide the eye to the distinct separation between the spinodal (shaded green) and IO (shaded yellow) morphologies.

As Si expands, the average values of σ_{max} and W increase until peaking at approximately 60 vol% expansion and then decrease, an unexpected behavior that we attribute to the softening of the lithiated Si and stress relaxation upon yielding, $\sigma_{\mathrm{vm}} \geq \sigma_{\mathrm{y}}$ in Fig. 3a. Both morphologies experience larger and broader σ_{max} and W distributions at 60 vol% expansion, which we theorize is due to the unique interplay of these properties at this critical point. Throughout the entire lithiation process, the IO displays higher average values and broader distributions that extend to larger maxima for both σ_{max} and W, and the σ_{max} of the IO is multimodal. For the spinodal morphologies, σ_{max} and W have a single narrow peak for the probability density, which we theorize

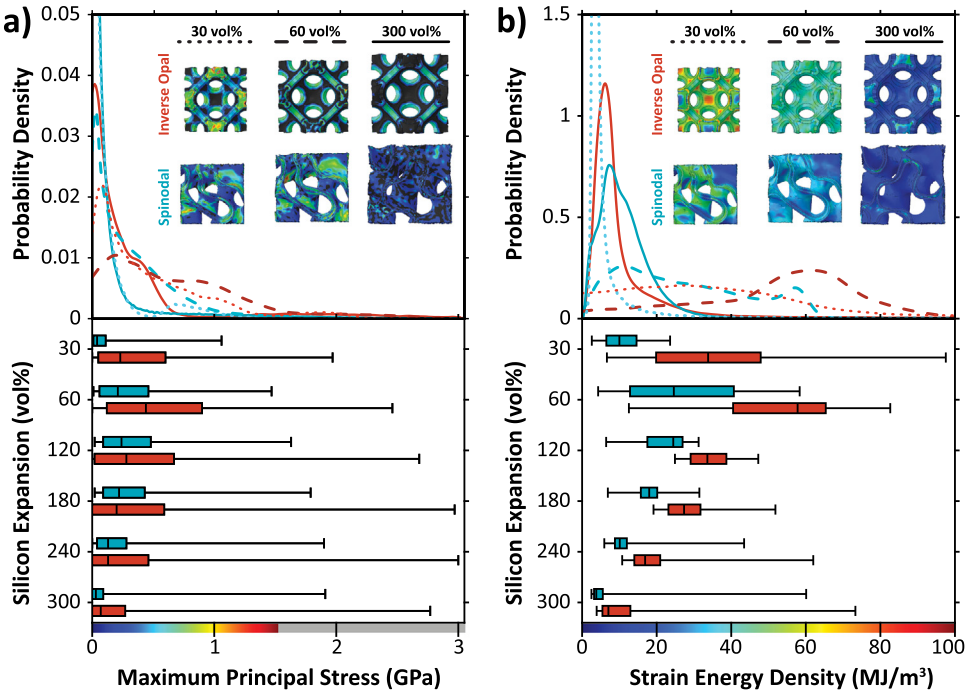

Fig. 2. (a) Maximum principal stress and (b) strain energy density, as silicon expands from an initial thickness of 100 nm for the inverse opal (red) and spinodal (blue). Top graphs show the probability density normalized by the area under the curve at 30 (dotted), 60 (dashed), and 300 (solid) vol% expansion, where insets are the contours on the models (color scale along the bottom x-axis). Bottom graphs are box and whisker plots, where the box denotes the 25th–75th percentile range, the internal line represents the median value, and the endcaps mark the 1st and 99th percentiles. For each Si vol% expansion, the top box plot is for the spinodal and bottom box plot is for the inverse opal. (For interpretation of the references to color in this figure legend, the reader is referred to the web version of this article.)

is due to its unique curvatures that distribute the stress and strain energy more evenly throughout the Si layer. Conversely, the IO experiences a large stress concentration and multimodal σ_{max} distribution due to the sharp curvature variations near the pore throats. As seen in the contours of Fig. 2a, the smaller pore size constricts the Si expansion and results in the buildup of high stresses that in turn push the Ni scaffold convex regions outwards, making the pore throat smaller, creating an even sharper curvature, and further exasperating the stress concentration, as previously shown in other IO studies [16,35]. In addition to the magnitude of stress, the large positive curvature in those regions can consequently make the IO more susceptible to cracking and delamination when compared to the spinodal morphology.

Our results show that 60 vol% expansion can be particularly problematic, especially for the IO. This can then get exacerbated upon cycling because initiated cracks and delamination in the Si can propagate and eventually lead to electrode failure. Thus, in the next section where we study the effect of Si thickness, we will focus on this point, as it is the most problematic in the process.

3.2. Effect of silicon layer thickness

Depending on the application, the thickness and overall volume content of Si can be varied in electrode design to balance gravimetric and volumetric power and energy densities. With increasing t_{Si}, the power density is limited by diffusion kinetics through the thickness, while the energy density increases with the overall volume of active material. Fig. 4 compares the σ_{max} and W for the IO and spinodal at 60 vol% expansion as a function of the Si layer thickness, t_{Si}, ranging from 50 nm to 150 nm.

Qualitatively, as t_{Si} is increased, there is less pore space for the Si to expand into, which results in an increase in σ_{max}. The trends for W vs. t_{Si} reverse during the lithiation process (Fig.S10) because they are convoluted by the nonlinear material properties of the Si alloy. However, between the models, the IO has a larger magnitude and broader distribution of σ_{max} and has a larger W for the entire range of Si thicknesses explored in this study. When looking at the contours in Fig. 4 and Fig.S11, as t_{Si} increases the gradient of σ_{max} and W through the thickness of Si increases, especially for the IO. As such, even though the σ_{max} increases with thickness, it is localized and the overall percentage of Si experiencing yielding decreases with t_{Si}, as seen in Fig. 3b. It is also interesting to note that the spinodal with t_{Si} of 150 nm has a similar range of σ_{max} as the IO with only a 50 nm coating, and similar trends are seen in Fig.S12 for 300 vol% expansion. In addition, the spinodal morphology appears to delay the onset of yielding as indicated by the intersection of the spinodal morphology σ_{vm} whisker plots with the σ_y line (Fig. 3a) at later Si volume expansion than the IO. The spinodal morphology also has a lower fraction of Si yielded than the IO throughout the lithiation process for all Si thicknesses as emphasized by the distinct separation between the shaded regions in Fig. 3b. This implies that an even thicker coating and thus larger energy density could be achieved by utilizing the spinodal morphology without enhancing degradation rates, and if smaller thicknesses are required for the application, a spinodal structure will be less susceptible to mechanical degradation than the IO.

3.3. Effect of curvature

Curvature can play a significant role in the distributions of stress and strain energy density during expansion [3,5,9], and we surmise that this is the primary cause of the differences seen between the spinodal and IO morphologies. In order to test this hypothesis, the two models will be compared to two triply periodic minimal surface (TPMS) structures—a gyroid and a Schwartz primitive, where the former closely resembles the spinodal and latter the IO. Fig. 5 shows the principal curvature maps for the Ni

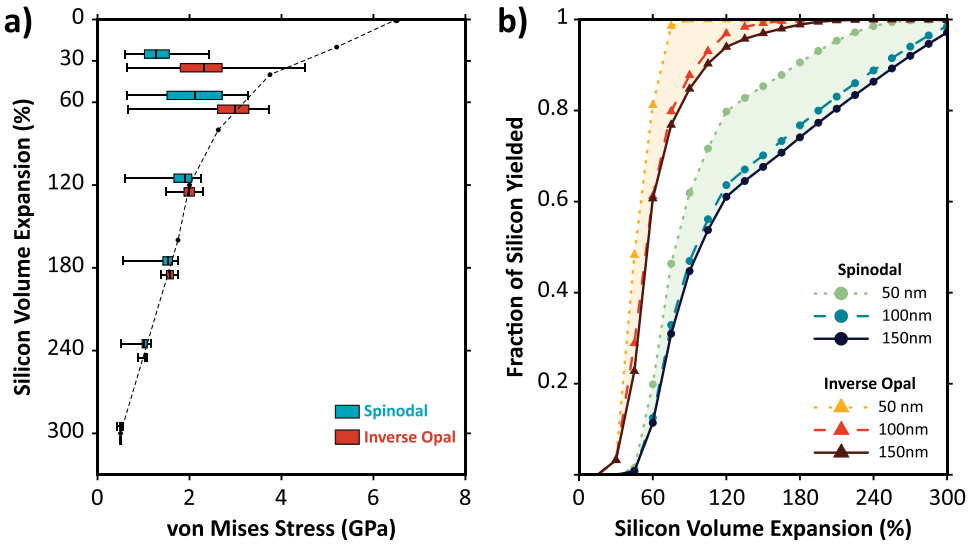

Fig. 3. Yielding behavior of silicon during expansion. (a) Whisker plots of von Mises stress for spinodal (blue, top box plot) and inverse opal (red, bottom box plot) with 100 nm Si thickness, where the end caps mark the 1st and 99th percentiles relative to the lithiation-dependent silicon yield strength (dashed line). (b) Fraction of silicon yielded for spinodal (circles) and inverse opal (triangles) for Si thickness of 50 nm (dotted), 100 nm (dashed), and 150 nm (solid). The shaded regions are to guide the eye. (For interpretation of the references to color in this figure legend, the reader is referred to the web version of this article.)

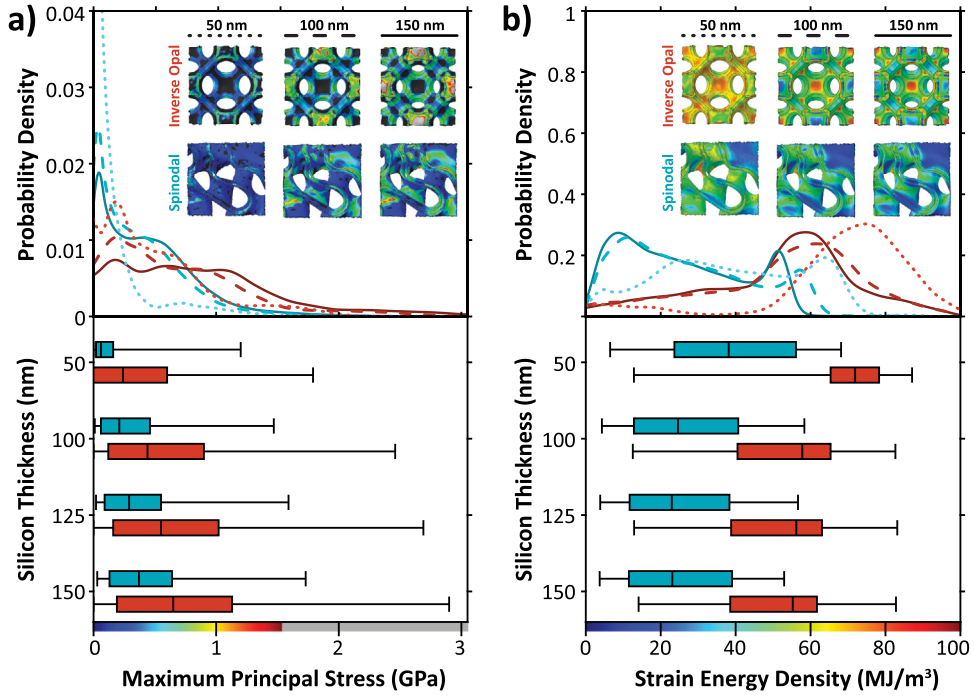

Fig. 4. (a) Maximum principal stress and (b) strain energy density for the inverse opal (red) and spinodal (blue) with 50, 100, 125, and 150 nm thick coatings of Si at 60 vol% expansion. Top graphs show the probability density normalized by the area under the curve for 50 (dotted), 100 (dashed), and 150 (solid) nm thick Si layers, where insets are the contours on the models (color scale along the bottom x-axis). Bottom graphs are box and whisker plots, where the box denotes the 25th–75th percentile range, the internal line represents the median value, and the endcaps mark the 1st and 99th percentiles. For each Si thickness, the top box plot is for the spinodal and bottom box plot is for the inverse opal. (For interpretation of the references to color in this figure legend, the reader is referred to the web version of this article.)

backbone surfaces and corresponding σ_{max} and W distributions at 300 vol% expansion for the spinodal (blue), IO (red), Schwartz primitive (purple), and gyroid (green) models with 100 nm thick Si coatings.

The shell structures of the spinodal, gyroid, and Schwartz primitive all have minimal surfaces such that each point on the surface should have a negative gaussian ($K < 0$) and zero mean ($H = 0$) curvature. The distributions in the principal curvature maps (Fig. 5c) for these morphologies are more dispersed than theorized because the curvatures were calculated from the Ni surface which is offset from the initial shell structures by 1 μm on either side; however, k_1 and k_2 are still aligned along the zero mean curvature line (white dashed line in Fig. 5c) and are within a negative gaussian curvature quadrant. Another key difference between the four morphologies is that the spinodal and gyroid have one characteristic curvature, and the Schwartz primitive and IO have two characteristic curvatures due to their pore throats. While the Schwartz primitive maintains a minimal surface ($k_1 =$

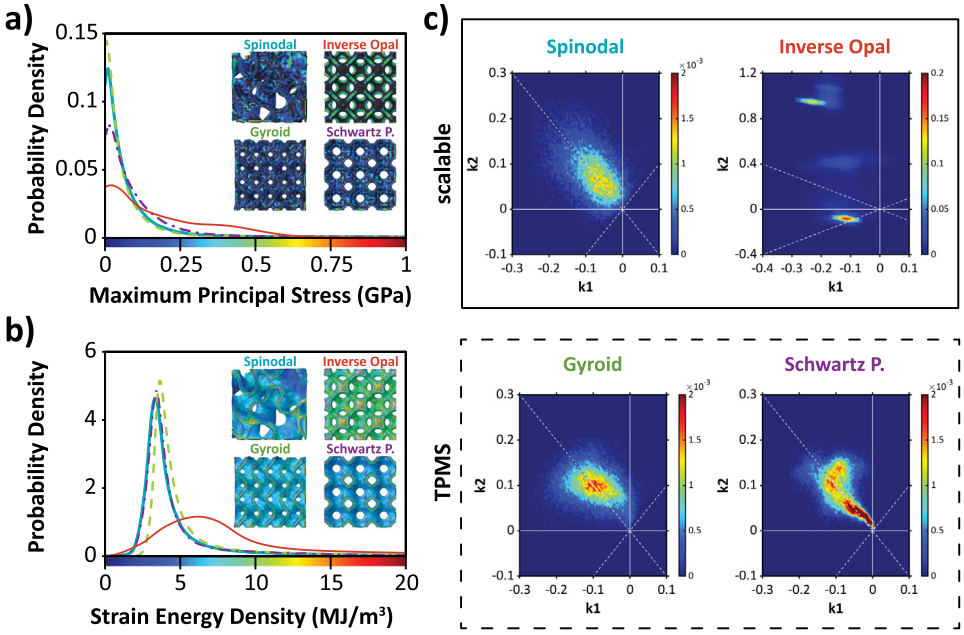

Fig. 5. Effect of curvature. Comparison between spinodal (blue thick solid line), inverse opal (red thin solid line), gyroid (green dashed line), and schwartz primitive (purple dash-dotted line) (a) maximum principal stress probability density distribution, (b) strain energy density probability distribution, and (c) principal curvatures. (For interpretation of the references to color in this figure legend, the reader is referred to the web version of this article.)

$-k_2$), the two curvatures of the IO correspond to the ellipsoidal regions ($-k_1$ and $-k_2$) generated by the templating particles, and the negative gaussian regions of the pore throats ($-k_1$ and $+k_2$).

From the σ_{max} (Fig. 5a) and W (Fig. 5b) distributions at 300 vol% expansion, it is clear that the minimal surfaces have narrower distributions and are centered along approximately the same values, while the IO has much larger magnitudes and broader distributions. The Schwartz primitive is similar to the IO in that it also has non-uniform pore sizes, but the balancing of k_1 and k_2 of the Schwartz primitive allows the stress and strain to be redistributed in such a way that σ_{max} and W are minimized. Conversely, for the IO, the positive k_2 is much larger in magnitude than the negative k_1. Therefore, although the pore throat exhibits a negative K, the large positive H leads to a stress concentration in that region, which could ultimately accelerate mechanical degradation. This is significant because (1) the σ_{max} and W can be drastically reduced by minimal surfaces even with pore throats, and (2) although negative K regions can alleviate these stresses, this is only applicable when H $\sim$ 0. Overall, the spinodal morphology has a predominance of both zero H and negative K values that allows it to approach the ideal behavior of the TPMS structures while also being amenable to self-assembly and scaleup. Our findings unveil the remarkable potential of materials derived from spinodal decomposition for next generation Li-ion battery electrodes and other porous material coatings that undergo large volumetric expansions.

4. Conclusions

In this work we conduct finite element analysis simulations to understand the effect of morphology on the mechanical degradation of Si-based Li-ion battery composite anodes, specifically spinodal and IO Ni backbones with Si coating thicknesses between 50 and 150 nm, as they undergo large volume expansion during lithiation. We compare the maximum principal stress and strain energy density distributions as indicators for cracking and delamination, respectively, and compare our results to gyroid and Schwartz primitive morphologies to understand the effects of interfacial curvature, periodicity, and pore uniformity on mechanical behavior. While our simulations do not incorporate cycling, crack modeling, or diffusion kinetics, they are able to highlight the importance of tailoring morphology to hinder mechanical degradation in Li-ion batteries. They also reveal that the point most prone to mechanical failure is at an intermediate lithiation state due to the unique evolution of the Si active layer material properties during lithiation. In summary, compared to the IO, we have shown that the spinodal morphology has lower and more uniformly distributed σ_{max} and W, and appears to delay the onset of expansion-induced yielding at all Si layer thicknesses, which we attribute to its unique curvature distribution. Our work unveils spinodal morphologies as particularly promising for the design of Li-ion battery electrodes and other porous material coatings undergoing volume variations, owing to their inherent ability to mitigate material degradation, while also being amendable to scalable synthesis.

Declaration of competing interest

The authors declare that they have no known competing financial interests or personal relationships that could have appeared to influence the work reported in this paper.

Acknowledgments

Funding for this work was partly provided by the National Aeronautics and Space Administration, USA Research Opportunities in Complex Fluids and Macromolecular Biophysics Program (80NSSC21K0897). S.J.G. acknowledges funding from the National Science Foundation, USA Graduate Research Fellowship Program (DGE-1839285). The ABAQUS Finite Element Analysis software is licensed from Dassault Systèmes SIMULIA, as part of a Strategic Academic Customer Program between UC Irvine and SIMULIA. The Simpleware ScanIP software is licensed from Synopsys by the Irvine Materials Research Institute (IMRI) at UC Irvine.

Appendix A. Supplementary data

Supplementary material related to this article can be found online at https://doi.org/10.1016/j.eml.2022.101746.

References

[1] H. Zhang, P.v. Braun, Three-dimensional metal scaffold supported bicontinuous silicon battery anodes, Nano Lett. 12 (2012) 2778–2783, http://dx.doi.org/10.1021/nl204551m.

[2] Z. Zheng, B. Chen, N. Fritz, Y. Gurumukhi, J. Cook, M.N. Ates, N. Miljkovic, P.V. Braun, P. Wang, The impact of non-uniform metal scaffolds on the performance of 3D structured silicon anodes, J. Energy Storage 30 (2020) 101502, http://dx.doi.org/10.1016/j.est.2020.101502.

[3] N.P. Mitchell, V. Koning, V. Vitelli, W.T.M. Irvine, Fracture in sheets draped on curved surfaces, Nature Mater. 16 (2017) 89–93, http://dx.doi.org/10.1038/nmat4733.

[4] N.P. Mitchell, Fracture in Sheets Draped on Curved Surfaces, in: Geometric Control of Fracture and Topological Metamaterials, Springer Nature 5 (2018) 86–96, http://dx.doi.org/10.1007/978-3-030-36361-1.

[5] J.W. Hutchinson, Delamination of compressed films on curved substrates, J. Mech. Phys. Solids 49 (2001) 1847–1864, http://dx.doi.org/10.1016/S0022-5096(01)00029-1.

[6] Z. Zheng, B. Chen, Y. Xu, N. Fritz, Y. Gurumukhi, J. Cook, M.N. Ates, N. Miljkovic, P.v. Braun, P. Wang, A Gaussian process-based crack pattern modeling approach for battery anode materials design, J. Electrochem. Energy Convers. Storage 18 (2021) http://dx.doi.org/10.1115/1.4046938.

[7] A.G. Evans, D.R. Clarke, C.G. Levi, The influence of oxides on the performance of advanced gas turbines, J. Eur. Ceram. Soc. 28 (2008) 1405–1419, http://dx.doi.org/10.1016/j.jeurceramsoc.2007.12.023.

[8] G. Qian, T. Nakamura, C.C. Berndt, Effects of thermal gradient and residual stresses on thermal barrier coating fracture, Mech. Mater. 27 (1998) 91–110, http://dx.doi.org/10.1016/S0167-6636(97)00042-2.

[9] Y. Ma, X. Liu, X. Yao, W. Hao, R. Zhang, D. Fang, Buckle-driven delamination of thermal barrier coatings on a polynomial curved substrate, Modelling Simulation Mater. Sci. Eng. 21 (2013) 055026, http://dx.doi.org/10.1088/0965-0393/21/5/055026.

[10] M.Y. He, A.G. Evans, J.W. Hutchinson, Effects of morphology on the decohesion of compressed thin films, Mater. Sci. Eng.: A 245 (1998) 168–181, http://dx.doi.org/10.1016/S0921-5093(97)00848-4.

[11] R.B. Heimann, Plasma-sprayed hydroxylapatite-based coatings: Chemical, mechanical, microstructural, and biomedical properties, J. Therm. Spray Technol. 25 (2016) 827–850, http://dx.doi.org/10.1007/S11666-016-0421-9, 2016 25:5.

[12] U. Sharma, D. Concagh, L. Core, Y. Kuang, C. You, Q. Pham, G. Zugates, R. Busold, S. Webber, J. Merlo, R. Langer, G.M. Whitesides, M. Palasis, The development of bioresorbable composite polymeric implants with high mechanical strength, Nature Mater. 17 (2018) 96–103, http://dx.doi.org/10.1038/nmat5016.

[13] Z.-L. Xu, X. Liu, Y. Luo, L. Zhou, J.-K. Kim, Nanosilicon anodes for high performance rechargeable batteries, Prog. Mater. Sci. 90 (2017) 1–44, http://dx.doi.org/10.1016/j.pmatsci.2017.07.003.

[14] N. Nitta, F. Wu, J.T. Lee, G. Yushin, Li-ion battery materials: Present and future, Mater. Today 18 (2015) 252–264, http://dx.doi.org/10.1016/j.mattod.2014.10.040.

[15] W. Tao, P. Wang, Y. You, K. Park, C.Y. Wang, Y.K. Li, F.F. Cao, S. Xin, Strategies for improving the storage performance of silicon-based anodes in lithium-ion batteries, Nano Res. 12 (2019) 1739–1749, http://dx.doi.org/10.1007/s12274-019-2361-4.

[16] Z. Zheng, B. Chen, N. Fritz, Y. Gurumukhi, J. Cook, M.N. Ates, N. Miljkovic, P. v. Braun, P. Wang, Lithiation induced stress concentration for 3D metal scaffold structured silicon anodes, J. Electrochem. Soc. 166 (2019) A2083–A2090, http://dx.doi.org/10.1149/2.1031910jes.

[17] L. Wang, T. Liu, X. Peng, W. Zeng, Z. Jin, W. Tian, B. Gao, Y. Zhou, P.K. Chu, K. Huo, L. Wang, T.F. Liu, W.W. Zeng, W.F. Tian, Y.H. Zhou, K.F. Huo, X. Peng, P.K. Chu, Z.Z. Jin, B. Gao, Highly stretchable conductive glue for high-performance silicon anodes in advanced lithium-ion batteries, Adv. Funct. Mater. 28 (2018) 1704858, http://dx.doi.org/10.1002/ADFM.201704858.

[18] Q. Xu, J.-Y. Li, J.-K. Sun, Y.-X. Yin, L.-J. Wan, Y.-G. Guo, Q. Xu, J.-Y. Li, J.-K. Sun, Y.-X. Yin, L.-J. Wan, Y.-G. Guo, Watermelon-inspired si/c microspheres with hierarchical buffer structures for densely compacted lithium-ion battery anodes, Adv. Energy Mater. 7 (2017) 1601481, http://dx.doi.org/10.1002/AENM.201601481.

[19] X. Zuo, J. Zhu, P. Müller-Buschbaum, Y.J. Cheng, Silicon based lithium-ion battery anodes: A chronicle perspective review, Nano Energy (2017) 113–143, http://dx.doi.org/10.1016/j.nanoen.2016.11.013.

[20] J.K. Dora, A. Sengupta, S. Ghosh, N. Yedla, J. Chakraborty, Stress evolution with concentration-dependent compositional expansion in a silicon lithium-ion battery anode particle, J. Solid State Electrochem. 23 (2019) 2331–2342, http://dx.doi.org/10.1007/s10008-019-04353-y.

[21] C.C. Hsieh, Y.G. Lin, C.L. Chiang, W.R. Liu, Carbon-coated porous Si/C composite anode materials via two-step etching/coating processes for lithium-ion batteries, Ceram. Int. 46 (2020) 26598–26607, http://dx.doi.org/10.1016/j.ceramint.2020.07.128.

[22] W. An, B. Xiang, J. Fu, S. Mei, S. Guo, K. Huo, X. Zhang, B. Gao, P.K. Chu, Three-dimensional carbon-coating silicon nanoparticles welded on carbon nanotubes composites for high-stability lithium-ion battery anodes, Appl. Surf. Sci. 479 (2019) 896–902, http://dx.doi.org/10.1016/j.apsusc.2019.02.145.

[23] B. Li, F. Yao, J.J. Bae, J. Chang, M.R. Zamfir, D.T. Le, D.T. Pham, H. Yue, Y.H. Lee, Hollow carbon nanospheres/silicon/alumina core–shell film as an anode for lithium-ion batteries, Sci. Rep. 5 (2015) 7659, http://dx.doi.org/10.1038/srep07659.

[24] L. Cui, Y. Yang, C. Hsu, Y. Cui, Carbon - silicon core - shell nanowires as high capacity electrode for lithium ion batteries, Nano Letters 9 (2009) 3370–3374, http://dx.doi.org/10.1021/nl901670t.

[25] S. Chen, L. Shen, P.A. van Aken, J. Maier, Y. Yu, Dual-functionalized double carbon shells coated silicon nanoparticles for high performance lithium-ion batteries, Adv. Mater. 29 (2017) 1605650, http://dx.doi.org/10.1002/adma.201605650.

[26] T. Shen, X.H. Xia, D. Xie, Z.J. Yao, Y. Zhong, J.Y. Zhan, D.H. Wang, J.B. Wu, X.L. Wang, J.P. Tu, Encapsulating silicon nanoparticles into mesoporous carbon forming pomegranate-structured microspheres as a high-performance anode for lithium ion batteries, J. Mater. Chem. A 5 (2017) 11197–11203, http://dx.doi.org/10.1039/c7ta03294c.

[27] Y. He, F. Han, F. Wang, J. Tao, H. Wu, F. Zhang, J. Liu, Optimal microstructural design of pitch-derived soft carbon shell in yolk-shell silicon/carbon composite for superior lithium storage, Electrochim. Acta 373 (2021) 137924, http://dx.doi.org/10.1016/j.electacta.2021.137924.

[28] S.A. Klankowski, R.A. Rojeski, B.A. Cruden, J. Liu, J. Wu, J. Li, A high-performance lithium-ion battery anode based on the core–shell heterostructure of silicon-coated vertically aligned carbon nanofibers, J. Mater. Chem. A 1 (2013) 1055–1064, http://dx.doi.org/10.1039/c2ta00057a.

[29] F. Dou, L. Shi, G. Chen, D. Zhang, Silicon/carbon composite anode materials for lithium-ion batteries, Electrochem. Energy Rev. 2 (1918) 149–198, http://dx.doi.org/10.1007/s41918-018-00028-w.

[30] B.F. Song, A. Dhanabalan, S.L. Biswal, Evaluating the capacity ratio and prelithiation strategies for extending cyclability in porous silicon composite anodes and lithium iron phosphate cathodes for high capacity lithium-ion batteries, J. Energy Storage 28 (2020) 101268, http://dx.doi.org/10.1016/J.EST.2020.101268.

[31] H.J. Shin, J.Y. Hwang, H.J. Kwon, W.J. Kwak, S.O. Kim, H.S. Kim, H.G. Jung, Sustainable encapsulation strategy of silicon nanoparticles in microcarbon sphere for high-performance lithium-ion battery anode, ACS Sustain. Chem. Eng. 8 (2020) 14150–14158, http://dx.doi.org/10.1021/acssuschemeng.0c04828.

[32] X.H. Liu, L. Zhong, S. Huang, S.X. Mao, T. Zhu, J.Y. Huang, Size-dependent fracture of silicon nanoparticles during lithiation, ACS Nano 6 (2012) 1522–1531, http://dx.doi.org/10.1021/nn204476h.

[33] J.M. Kim, V. Guccini, K. dong Seong, J. Oh, G. Salazar-Alvarez, Y. Piao, Extensively interconnected silicon nanoparticles via carbon network derived from ultrathin cellulose nanofibers as high performance lithium ion battery anodes, Carbon 118 (2017) 8–17, http://dx.doi.org/10.1016/j.carbon.2017.03.028.

[34] B. Hu, X. Kuang, S. Xu, X. Wang, A novel strategy for lithium-ion battery anode with enhanced cycling performance: Silicon particles enclosed in shell-like Mxenes/CNTs nanostructure, in: 2019 IEEE 32nd International Conference on Micro Electro Mechanical Systems (MEMS), IEEE, 2019, pp. 946–949, http://dx.doi.org/10.1109/MEMSYS.2019.8870669.

[35] Z. Zheng, B. Chen, N. Fritz, Y. Gurumukhi, J. Cook, M.N. Ates, N. Miljkovic, P. v. Braun, P. Wang, The impact of non-uniform metal scaffolds on the performance of 3D structured silicon anodes, J. Energy Storage 30 (2020) 101502, http://dx.doi.org/10.1016/j.est.2020.101502.

[36] H. Jia, X. Li, J. Song, X. Zhang, L. Luo, Y. He, B. Li, Y. Cai, S. Hu, X. Xiao, C. Wang, K.M. Rosso, R. Yi, R. Patel, J.G. Zhang, Hierarchical porous silicon structures with extraordinary mechanical strength as high-performance lithium-ion battery anodes, Nature Commun. 11 (2020) 1–9, http://dx.doi.org/10.1038/s41467-020-15217-9.

[37] A. Franco Gonzalez, N.H. Yang, R.S. Liu, Silicon anode design for lithium-ion batteries: Progress and perspectives, J. Phys. Chem. C 121 (2017) 27775–27787, http://dx.doi.org/10.1021/acs.jpcc.7b07793.

[38] B. Wang, J. Ryu, S. Choi, X. Zhang, D. Pribat, X. Li, L. Zhi, S. Park, R.S. Ruoff, Ultrafast-charging silicon-based coral-like network anodes for lithium-ion batteries with high energy and power densities(SI), ACS Nano 13 (2019) 2307–2315, http://dx.doi.org/10.1021/acsnano.8b09034.

[39] W. An, B. Gao, S. Mei, B. Xiang, J. Fu, L. Wang, Q. Zhang, P.K. Chu, K. Huo, Scalable synthesis of ant-nest-like bulk porous silicon for high-performance lithium-ion battery anodes, Nature Commun. 10 (2019) 1–11, http://dx.doi.org/10.1038/s41467-019-09510-5.

[40] M. Thakur, R.B. Pernites, N. Nitta, M. Isaacson, S.L. Sinsabaugh, M.S. Wong, S.L. Biswal, Freestanding macroporous silicon and pyrolyzed polyacrylonitrile as a composite anode for lithium ion batteries, Chem. Mater. 24 (2012) 2998–3003, http://dx.doi.org/10.1021/cm301376t.
[41] W. Luo, C. Fang, X. Zhang, J. Liu, H. Ma, G. Zhang, Z. Liu, X. Li, In situ generated carbon nanosheet-covered micron-sized porous si composite for long-cycling life lithium-ion batteries, ACS Appl. Energy Mater. 4 (2021) 535–544, http://dx.doi.org/10.1021/acsaem.0c02445.
[42] H. Wang, W. Tang, L. Ni, W. Ma, G. Chen, N. Zhang, X. Liu, R. Ma, Synthesis of silicon nanosheets from kaolinite as a high-performance anode material for lithium-ion batteries, J. Phys. Chem. Solids 137 (2020) 109227, http://dx.doi.org/10.1016/J.JPCS.2019.109227.
[43] Z. Fan, Y. Wang, S. Zheng, K. Xu, J. Wu, S. Chen, J. Liang, A. Shi, Z. Wang, A submicron Si@C core–shell intertwined with carbon nanowires and graphene nanosheet as a high-performance anode material for lithium ion battery, Energy Storage Mater. 39 (2021) 1–10, http://dx.doi.org/10.1016/J.ENSM.2021.04.005.
[44] N. Harpak, G. Davidi, Y. Melamed, A. Cohen, F. Patolsky, Self-catalyzed vertically aligned carbon nanotube-silicon core-shell array for highly stable, high-capacity lithium-ion batteries, Langmuir 36 (2020) 889–896, http://dx.doi.org/10.1021/acs.langmuir.9b03424.
[45] Y. Zhuo, H. Sun, M.H. Uddin, M.K.S. Barr, D. Wisser, P. Rozmann, J.D. Esper, S. Tymek, D. Döhler, W. Peukert, M. Hartmann, J. Bachmann, An additive-free silicon anode in nanotube morphology as a model lithium ion battery material, Electrochim. Acta 388 (2021) 138522, http://dx.doi.org/10.1016/J.ELECTACTA.2021.138522.
[46] Z. Zhang, X. Han, L. Li, P. Su, W. Huang, J. Wang, J. Xu, C. Li, S. Chen, Y. Yang, Tailoring the interfaces of silicon/carbon nanotube for high rate lithium-ion battery anodes, J. Power Sources 450 (2020) 227593, http://dx.doi.org/10.1016/J.JPOWSOUR.2019.227593.
[47] B. Wang, J. Ryu, S. Choi, X. Zhang, D. Pribat, X. Li, L. Zhi, S. Park, R.S. Ruoff, Ultrafast-charging silicon-based coral-like network anodes for lithium-ion batteries with high energy and power densities, ACS Nano 13 (2019) http://dx.doi.org/10.1021/acsnano.8b09034, acsnano.8b09034.
[48] H. Ching, T.J. Thorson, B. Paul, A. Mohraz, Rapid production of bicontinuous macroporous materials using intrinsically polymerizable bijels, Mater. Adv. 2 (2021) 5067–5075, http://dx.doi.org/10.1039/D1MA00404B.
[49] E.M. Herzig, K.A. White, A.B. Schofield, W.C.K. Poon, P.S. Clegg, Bicontinuous emulsions stabilized solely by colloidal particles, Nature Mater. 6 (2007) 966–971, http://dx.doi.org/10.1038/nmat2055.
[50] T. Wada, K. Yubuta, H. Kato, Evolution of a bicontinuous nanostructure via a solid-state interfacial dealloying reaction, Scr. Mater. 118 (2016) 33–36, http://dx.doi.org/10.1016/J.SCRIPTAMAT.2016.03.008.
[51] P.A. Geslin, I. McCue, B. Gaskey, J. Erlebacher, A. Karma, Topology-generating interfacial pattern formation during liquid metal dealloying, Nature Commun. 6 (2015) 1–8, http://dx.doi.org/10.1038/ncomms9887.
[52] P.S. Clegg, J.H.J. Thijssen, Bijels: Bicontinuous Particle-Stabilized Emulsions, Royal Society of Chemistry, Cambridge, 2020, http://dx.doi.org/10.1039/9781839160974.
[53] H. Jinnai, Y. Nishikawa, T. Hashimoto, Curvature distributions of spinodal interface in a condensed matter system, Phys. Rev. E 59 (1999) R2554–R2557, http://dx.doi.org/10.1103/PhysRevE.59.R2554.
[54] M.E. Cates, P.S. Clegg, Bijels: a new class of soft materials, Soft Matter 4 (2008) 2132–2138, http://dx.doi.org/10.1039/B807312K.
[55] E.M. Herzig, K.A. White, A.B. Schofield, W.C.K. Poon, P.S. Clegg, Bicontinuous emulsions stabilized solely by colloidal particles, Nature Mater. 6 (2007) 966–971, http://dx.doi.org/10.1038/nmat2055.
[56] M.N. Lee, A. Mohraz, Bicontinuous macroporous materials from Bijel templates, Adv. Mater. 22 (2010) 4836–4841, http://dx.doi.org/10.1002/ADMA.201001696.
[57] M.T. Hsieh, B. Endo, Y. Zhang, J. Bauer, L. Valdevit, The mechanical response of cellular materials with spinodal topologies, J. Mech. Phys. Solids 125 (2019) 401–419, http://dx.doi.org/10.1016/J.JMPS.2019.01.002.
[58] S.J. Gross, K.M. McDevitt, D.R. Mumm, A. Mohraz, Mitigating bubble traffic in gas-evolving electrodes via spinodally derived architectures, ACS Appl. Mater. Interfaces 13 (2021) 8537, http://dx.doi.org/10.1021/acsami.0c20798.
[59] K.M. Mcdevitt, D.R. Mumm, A. Mohraz, Improving cyclability of ZnO electrodes through microstructural design, ACS Appl. Energy Mater. 2 (2019) 8107–8117, http://dx.doi.org/10.1021/acsaem.9b01584.
[60] J.A. Witt, D.R. Mumm, A. Mohraz, Microstructural tunability of co-continuous bijel-derived electrodes to provide high energy and power densities, J. Mater. Chem. A 4 (2016) 1000–1007, http://dx.doi.org/10.1039/C5TA06260H.
[61] Y. Zhang, M.-T. Hsieh, L. Valdevit, Mechanical performance of 3D printed interpenetrating phase composites with spinodal topologies, Compos. Struct. 263 (2021) 113693, http://dx.doi.org/10.1016/j.compstruct.2021.113693.
[62] M.-T. Hsieh, M.R. Begley, L. Valdevit, Architected implant designs for long bones: Advantages of minimal surface-based topologies, Mater. Des. 207 (2021) 109838, http://dx.doi.org/10.1016/j.matdes.2021.109838.
[63] A. Torrents, T.A. Schaedler, A.J. Jacobsen, W.B. Carter, L. Valdevit, Characterization of nickel-based microlattice materials with structural hierarchy from the nanometer to the millimeter scale, Acta Mater. 60 (2012) 3511–3523, http://dx.doi.org/10.1016/j.actamat.2012.03.007.
[64] M. Hsieh, B. Endo, Y. Zhang, J. Bauer, L. Valdevit, Journal of the mechanics and physics of solids the mechanical response of cellular materials with spinodal topologies, J. Mech. Phys. Solids 125 (2019) 401–419, http://dx.doi.org/10.1016/j.jmps.2019.01.002.
[65] A. Torrents, T.A. Schaedler, A.J. Jacobsen, W.B. Carter, L. Valdevit, Characterization of nickel-based microlattice materials with structural hierarchy from the nanometer to the millimeter scale, Acta Mater. 60 (2012) 3511–3523, http://dx.doi.org/10.1016/j.actamat.2012.03.007.
[66] A.G. Izard, J. Bauer, C. Crook, V. Turlo, L. Valdevit, Ultrahigh energy absorption multifunctional spinodal nanoarchitectures, Small 15 (2019) 1903834, http://dx.doi.org/10.1002/smll.201903834.
[67] H. Yu, J.W. Hutchinson, Delamination of thin film strips, Thin Solid Films 423 (2003) 54–63, http://dx.doi.org/10.1016/S0040-6090(02)00973-2.
[68] K. Shu, C. Zhang, D. Zheng, S. Cui, P. Hou, L. Gu, Analysis on the cracking of thin hard films considering the effects of interfacial delamination, Surf. Coat. Technol. 402 (2020) http://dx.doi.org/10.1016/j.surfcoat.2020.126284.
[69] S. Pal, S.S. Damle, S.H. Patel, M.K. Datta, P.N. Kumta, S. Maiti, Modeling the delamination of amorphous-silicon thin film anode for lithium-ion battery, J. Power Sources 246 (2014) 149–159, http://dx.doi.org/10.1016/j.jpowsour.2013.06.089.
[70] A.G. Evans, D.R. Mumm, J.W. Hutchinson, G.H. Meier, F.S. Pettit, Mechanisms controlling the durability of thermal barrier coatings, Prog. Mater. Sci. 46 (2001) 505–553, http://dx.doi.org/10.1016/S0079-6425(00)00020-7.
[71] L. Chen, P. Wu, P. Song, J. Feng, Potential thermal barrier coating materials: RE_3NbO_7 (RE=La, Nd, Sm, Eu, Gd, Dy) ceramics, J. Am. Ceram. Soc. 101 (2018) 4503–4508, http://dx.doi.org/10.1111/JACE.15798.
[72] Y. Pan, D. Pu, Y. Jia, Adjusting the correlation between the oxidation resistance and mechanical properties of Pt-based thermal barrier coating, Vacuum 172 (2020) 109067, http://dx.doi.org/10.1016/J.VACUUM.2019.109067.
[73] D. Li, P. Jiang, R. Gao, F. Sun, X. Jin, X. Fan, Experimental and numerical investigation on the thermal and mechanical behaviours of thermal barrier coatings exposed to CMAS corrosion, J. Adv. Ceram. 10 (2021) 551–564, http://dx.doi.org/10.1007/S40145-021-0457-2.
[74] X.Y. Sun, G.K. Xu, X. Li, X.Q. Feng, H. Gao, Mechanical properties and scaling laws of nanoporous gold, J. Appl. Phys. 113 (2013) 023505, http://dx.doi.org/10.1063/1.4774246.
[75] M. Meyer, M. Desbrun, P. Schröder, A.H. Barr, Discrete Differential-Geometry Operators for Triangulated 2-Manifolds, Springer, Berlin, Heidelberg, 2003, pp. 35–57, http://dx.doi.org/10.1007/978-3-662-05105-4_2.
[76] S. Chen, A. Du, C. Yan, Molecular dynamic investigation of the structure and stress in crystalline and amorphous silicon during lithiation, Comput. Mater. Sci. 183 (2020) 109811, http://dx.doi.org/10.1016/J.COMMATSCI.2020.109811.
[77] V.B. Shenoy, P. Johari, Y. Qi, Elastic softening of amorphous and crystalline Li-Si Phases with increasing Li concentration: A first-principles study, J. Power Sources 195 (2010) 6825–6830, http://dx.doi.org/10.1016/j.jpowsour.2010.04.044.
[78] F. Fan, S. Huang, H. Yang, M. Raju, D. Datta, V.B. Shenoy, A.C.T. van Duin, S. Zhang, T. Zhu, Mechanical properties of amorphous Li x Si alloys: a reactive force field study, Modelling Simul. Mater. Sci. Eng. 21 (2013) 074002, http://dx.doi.org/10.1088/0965-0393/21/7/074002.
[79] Z. Cui, F. Gao, Z. Cui, J. Qu, A second nearest-neighbor embedded atom method interatomic potential for Li–Si alloys, J. Power Sources 207 (2012) 150–159, http://dx.doi.org/10.1016/j.jpowsour.2012.01.145.
[80] K. Zhao, G.A. Tritsaris, M. Pharr, W.L. Wang, O. Okeke, Z. Suo, J.J. Vlassak, E. Kaxiras, Reactive flow in silicon electrodes assisted by the insertion of lithium, Nano Lett. 12 (2012) 4397–4403, http://dx.doi.org/10.1021/nl302261w.
[81] M. Gu, Y. He, J. Zheng, C. Wang, Nanoscale silicon as anode for Li-ion batteries: The fundamentals, promises, and challenges, Nano Energy 17 (2015) 366–383, http://dx.doi.org/10.1016/J.NANOEN.2015.08.025.
[82] L.C. Loaiza, L. Monconduit, V. Seznec, L.C. Loaiza, V. Seznec, L. Monconduit, Si and Ge-based anode materials for Li-, Na-, and K-ion batteries: A perspective from structure to electrochemical mechanism, Small 16 (2020) 1905260, http://dx.doi.org/10.1002/SMLL.201905260.
[83] H. Yang, F. Fan, W. Liang, X. Guo, T. Zhu, S. Zhang, A chemo-mechanical model of lithiation in silicon, J. Mech. Phys. Solids 70 (2014) 349–361, http://dx.doi.org/10.1016/J.JMPS.2014.06.004.
[84] H. Wang, H.B. Chew, Molecular dynamics simulations of plasticity and cracking in lithiated silicon electrodes, Extreme Mech. Lett. 9 (2016) 503–513, http://dx.doi.org/10.1016/j.eml.2016.02.020.
[85] L. Yang, H.-S. Chen, H. Jiang, Y.-J. Wei, W.-L. Song, D.-N. Fang, Failure mechanisms of 2D silicon film anodes: in situ observations and simulations on crack evolution, Chem. Commun. 54 (2018) 3997–4000, http://dx.doi.org/10.1039/C7CC09708E.

[86] H. Sitinamaluwa, J. Nerkar, M. Wang, S. Zhang, C. Yan, Deformation and failure mechanisms of electrochemically lithiated silicon thin films, RSC Adv. 7 (2017) 13487–13497, http://dx.doi.org/10.1039/c7ra01399j.
[87] Z.Y. Wei, H.N. Cai, C.J. Li, Comprehensive dynamic failure mechanism of thermal barrier coatings based on a novel crack propagation and TGO growth coupling model, Ceram. Int. 44 (2018) 22556–22566, http://dx.doi.org/10.1016/J.CERAMINT.2018.09.028.
[88] Q.M. Yu, L. Cen, Y. Wang, Numerical study of residual stress and crack nucleation in thermal barrier coating system with plane model, Ceram. Int. 44 (2018) 5116–5123, http://dx.doi.org/10.1016/J.CERAMINT.2017.12.112.
[89] E.P. Busso, Z.Q. Qian, M.P. Taylor, H.E. Evans, The influence of bondcoat and topcoat mechanical properties on stress development in thermal barrier coating systems, Acta Mater. 57 (2009) 2349–2361, http://dx.doi.org/10.1016/J.ACTAMAT.2009.01.017.